2021 43rd Annual International Conference of the
IEEE Engineering in Medicine & Biology Society (EMBC)
Oct 31 - Nov 4, 2021. Virtual Conference

Effects of the 3D Geometry Reconstruction on the Estimation of 3D Porous Scaffold Permeability*.

Daniele Guarnera, Federica Iberite, Marco Piazzoni, Irini Gerges, Tommaso Santaniello, Lorenzo Vannozzi, Cristina Lenardi and Leonardo Ricotti

***Abstract* - 3D scaffolds for tissue engineering typically need to adopt a dynamic culture to foster cell distribution and survival throughout the scaffold. It is, therefore, crucial to know fluids' behavior inside the scaffold architecture, especially for complex porous ones. Here we report a comparison between simulated and measured permeability of a porous 3D scaffold, focusing on different modeling parameters. The scaffold features were extracted by micro-computed tomography (µCT) and representative volume elements were used for the computational fluid-dynamic analyses. The objective was to investigate the sensitivity of the model to the degree of detail of the µCT image and the elements of the mesh. These findings highlight the pros and cons of the modeling strategy adopted and the importance of such parameters in analyzing fluid behavior in 3D scaffolds.**

I. Introduction

The design of three-dimensional (3D) scaffolds is crucial for an effective tissue engineering of musculoskeletal tissues. To achieve 3D constructs, a possible strategy consists of developing microporous matrices. The internal architecture of these materials (mainly their porosity, pore size, and pore interconnectivity), influences the mechanical and mass transport properties of porous 3D scaffolds [1, 2]. These features, together with the pore distribution and orientation, determine if the scaffold permits a flow throughout the pores. The property encompassing all these features is known as permeability, a parameter that is independent of the fluid permeating the material [3, 4].

An appropriate permeability is crucial to enable nutrients transport, waste removal, and thus cell survival and growth within the scaffold [5 - 7]. Scaffold permeability is directly linked to the scaffold architecture, which can strongly influence cell behavior: it is known that pore size and scaffold porosity can affect cell viability and proliferation *in vitro* [8], or resident cell colonization and migration *in vivo* [9]. Various methods exist for the fabrication of porous scaffolds, including electrospinning, salt leaching and gas foaming. Reliable virtual models often help an appropriate control of these processes [10].

One of the most effective strategies to assess the scaffold internal architecture is the micro-computed tomography (μCT), which is non-invasive and non-destructive. μCT generates a sequence of high-resolution images of a sample through an X-ray source. The post-processing imaging allows a 3D reconstruction of the sample and the consequent analysis of the aforementioned architecture-related parameters. Furthermore, the 3D images are a key input for computational fluid-dynamic (CFD) simulations on the scaffold.

CFD simulations have been recently used to provide quantitative predictions on scaffold properties, such as permeability and wall shear stress [11-14], but also to predict the impact of such parameters on cell behavior [15, 16]. Computational models have been also used to optimize the internal structure of the scaffold from the mechanical properties standpoint and in the evaluation of the structural aspects on the flow parameters [17, 18]. However, CFD analyses of 3D scaffolds are often prohibitive from the computational cost viewpoint, when μCT-derived architectures must be managed, especially due to the scaffold's complex geometry. Indeed, the outputs of μCT are usually large-size files that require time-consuming pre-processing activities. μCT output files can require hard efforts in reducing the file size and solving the geometry errors that arise from complexity reduction. In addition, meshing, computation, and post-processing times must be taken into account in the case of highly non-homogeneous scaffolds [19, 20]. To overcome these issues, computational analyses are sometimes focused on one or more representative volume elements (RVE) [19, 21]: this strategy allows for shorter simulation times, but it could affect the final result when the pre-processing procedures are not accurately investigated.

The aim of this work is to investigate the RVE-CAD degree of the finish, the spatial position and size of the meshing elements, and to evaluate the effect of these features on the predicted permeability with respect to the measured one.

II. Materials and Methods

A. Scaffold fabrication

Mixture A (polyols): 16.00g PEG 2000 (Sigma Aldrich, 99%, 79.46 pphp); Glycerol 1.72g (Sigma Aldrich, ≥99% (GC), 8.57 pphp) and 2.4g MilliQ water (11.96 pphp).

Component B (polyisocyanate): 63.87 g Tolonate™ X FLO 100 (Vencorex, ≥99%). NCO index = 100.

Component C (catalyst): 0.38 g Dibutiltindilaurate DBTL (Sigma Aldrich, ≥ 96.0 %). %DBTL = 0.5% w/w.

* This work received both financial and technical support by INAIL, in the framework of the project MIO-PRO (Engineered patient-specific muscles for the restoration of myoelectric channels and prosthesis control).

D. Guarnera, F. Iberite, L. Vannozzi and L. Ricotti are with Scuola Superiore Sant'Anna, The Biorobotics Institute, Pontedera, Italy (corresponding author email: daniele.guarnera@santannapisa.it).

I. Gerges is with Tensive s.r.l., Milan, Italy.

M.Piazzoni, T. Santaniello and C. Lenardi are with University of Milan, Milan, Italy.

The mixture A was introduced in a 2L-PP rectangular container endowed with a lid, then placed in the oven at 85°C for at least 30 min. The temperature of mixture A was 80°C when components B and C were added. The resulting compound was mechanically mixed at 300 rpm for 30 s, then left raising for 1 min, until the expansion was arrested due to crosslinking. The final volume of the expanded foam was 1.4 l. The nominal density was 60.23 kg/m3. The raw foam was kept in the oven at 40 °C for 24 h to complete the curing process. Cylindrical samples were cut and purified according to the procedure previously described in Gerges et. al. [22].

B. Permeability test

The permeability k of the scaffold is a feature directly connected with the degree of pore interconnectivity. As mentioned above, it influences the scaffold ability to sustain cell growth and tissue regeneration. The permeability is described by the Darcy's law:

$$k = \eta \frac{Q}{A} \frac{L}{\Delta P} \quad (1)$$

where k is the intrinsic permeability in m^2, η is the kinematic viscosity of the fluid in Pa×s, Q is the volumetric flow rate in m^3/s, A is the scaffold cross-sectional area in m^2, L is the scaffold total length in m, and ΔP is the pressure drop over the scaffold in Pa. The constant pressure gradient method was adopted for assessing the experimental scaffold permeability, using the set-up depicted in Fig. 1. The volumetric flow rate Q of water (ρ_{water} = 998 kg/m^3 and $\eta_{water} = 8.9\times10^{-4}$ Pa×s) through the scaffold was measured as the mass of water crossing the scaffold over 60 s.

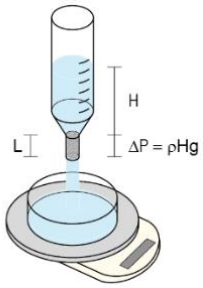

Fig. 1. Schematic representation of the experimental set-up used for permeability measurements.

Four independent samples were tested and each scaffold was tested three times (total measurement time = 20 min; sampling rate = 1 min). The mass was measured using a balance Radwag WLC 20/A2 with a precision of 0.1 g. The hydrostatic pressure was kept constant on the scaffold. By calculating $\Delta P = \rho_{water}\, g\, H$, being H the height of the water above the sample (in m) and g the gravitational acceleration, the intrinsic permeability k was determined.

C. μCT image analysis

Microtomography was used to analyze the pore distribution and the trabecular network of the scaffold 3D structure shown in Fig. 2(a). The files obtained from the μCT were used to set up the computational model. They were obtained through a customized cone beam system known as TomoLab [23] (cone beam energy = 40 kV, power = 200 µA, exposition time = 1.5 s). The dimension of the tomographic projections was 2004 × 1335 pixels and the final resolution was 8 μm. The slices reconstruction and correction were carried out through the software Cobra Exxim and the binary processing of the images was accomplished according to the method proposed in [24]. The combination between the plug-in BoneJ [25, 26] and the software Amira [27] was used to generate the images and analyze them. The sample extracted and analyzed was a volume of 1000 pixel per side (8 mm), as visible in Fig. 2 (b). The results in terms of the porous morphology of the scaffold extracted from the μCT files are summarized in Table I. The anisotropy degree specifies the tendency of the pore to be spherical (0 = completely spherical, 1 = maximum anisotropy), while the connection density indicates how much the structures are interconnected.

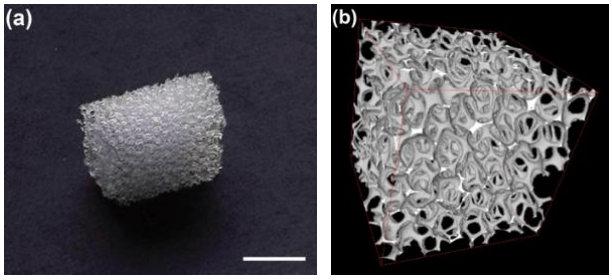

Fig. 2. (a) Photo of the porous scaffold. Scale bar = 500 µm. (b) Micro-computed tomography image of the porous scaffold used for the analysis. Sample side dimension = 8 mm.

TABLE I. SCAFFOLD MORPHOLOGY-RELATED PARAMETERS

Porosity %	93.3
Trabecular Thickness [μm]	138.0 ± 64.6
Pore Diameter [μm]	665.7 ± 129.0
Anisotropy Degree	0.3
Connection Density [μm^{-3}]	3 x 10^{-9}

D. Modeling strategy and flow characterization

The scaffold intrinsic permeability was simulated considering different RVEs, in the form of a rectangular box with one dimension equal to the scaffold length and a square section with a side dimension of 8.35×10^{-4} m. The RVEs were extracted from the μCT outputs and extensively reworked through the open-source softwares MeshLab [29], and Autodesk Fusion 360 [30]. These CAD files were then loaded in the CFD simulation tool to be modeled as fluid volumes. The process steps are introduced

in Fig. 3. A first assessment was based on an RVE at the center of the scaffold: here the permeability was evaluated by varying (i) the level of detail available in the input CAD, and (ii) the mesh refinement of the fluid volume. The CAD degree of the finish was related to the number of triangular polygons describing the scaffold, namely 22,000 (a), 11,000 (b), and 3,000 (c) (Fig. 3).

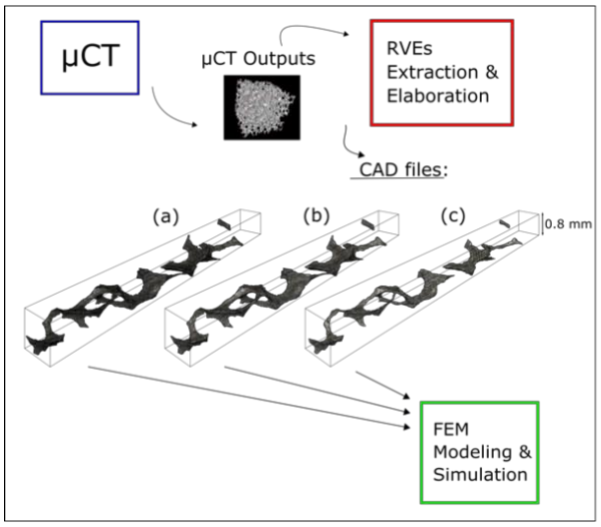

Fig. 3. Representation of the steps followed for permeability estimation. (a), (b) and (c) are RVEs with three different degrees of the finish, determined by the number of polygonal elements describing the scaffold, namely 22,000 (a), 11,000 (b), and 3,000 (c).

The tetrahedral elements considered for the mesh refinement of the fluid volume were 5.5×10^5, 3.1×10^6, and 1.1×10^7, respectively. The fluid was modeled as incompressible and Newtonian, with the properties of water as mentioned in Section II-B. COMSOL 5.6 was used to mesh the fluid volume and to solve the steady-state Navier-Stokes equations for laminar flow. A fixed pressure gap (724.49 Pa) was imposed between the extremities of the model, and no-slip conditions were imposed at the channel walls and the scaffold walls. The flow rate was computed by the software and used for the calculation of the intrinsic permeability through the Darcy's law (Eq. 1). The analysis was then performed on five different RVEs having the same dimensions (section $A = 7\times10^{-7}$ m^2, length $L = 8\times10^{-3}$ m) and representative of different locations of the scaffold. Their permeability was evaluated according to the boundary conditions expressed above. The RVEs distribution in the scaffold is shown in Fig. 4.

The machine used to run the CFD simulations held 32 GB of RAM memory and 8 cores.

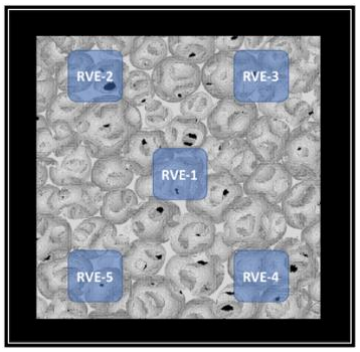

Fig. 4. Positions of five different RVEs in the scaffold (top view).

III. Results

The average scaffold intrinsic permeability obtained through the experimental tests was 1.71×10^{-9} m^2 (median value; 25th percentile = 1.58×10^{-9} m^2, 75th percentile = 1.93×10^{-9} m^2). The plot of the frequency distribution of the measured permeability is shown in Fig. 5.

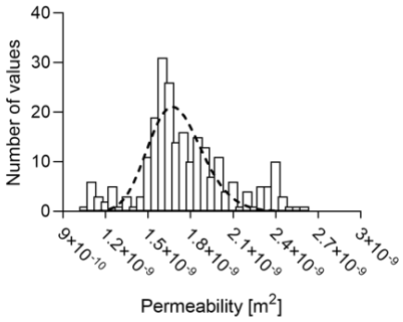

Fig. 5. Frequency distribution of the experimentally measured permeability (bin width = 5×10^{-11}). Dashed line: longnormal distribution.

The simulated permeability values, computed through the RVE extracted from the center of the scaffold, are summarized in Table II. The simulations were performed varying the degree of detail of the input CAD and the grid refinement.

TABLE II. VALUES OF SIMULATED PERMEABILITY IN M^2. THE SIMULATION TIME (IN MIN) IS REPORTED IN THE PARENTHESIS.

k ($\times 10^{-9}$) [m^2]	**Number of tetrahedral elements of the mesh**		
Number of CAD triangular polygons	**5.5×10^5**	**3.1×10^6**	**1.1×10^7**
22,000 (a)	1.90 (5 min)	2.05 (18 min)	2.10 (61 min)
11,000 (b)	1.93 (5 min)	2.09 (19 min)	2.14 (65 min)
3,000 (c)	2.64 (7 min)	2.89 (17 min)	2.95 (65 min)

Fig. 6 reports the absolute error between the simulation predictions (in Table II) and the experimental average

permeability value. A strong dependency from the CAD number of triangular polygons can be observed. From Fig. 6, the following considerations also emerge: *(i)* a medium degree of the finish (11,000 triangular polygons) was enough to describe accurately the scaffold geometry; *(ii)* the results accuracy was affected by the number of tetrahedral elements. The variation of the results with the increasing of the grid refinement suggested the necessity of more than 10^6 tetrahedral elements to accomplish a rather stable reliability.

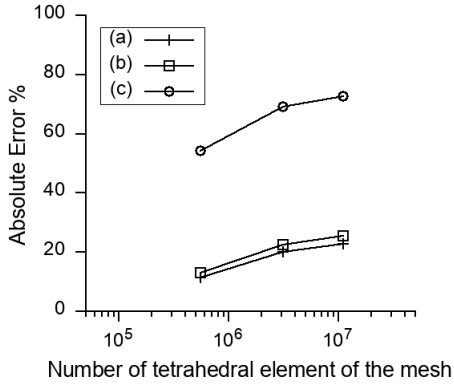

Fig. 6. Absolute error (%) between the simulated permeability values and the experimental ones for different degrees of the finish of the CAD model: (a) 22,000, (b) 11,000, and (c) 3,000, and for different degrees of refinement of the mesh.

The considerations expressed above drove the modeling features to be used for the following assessment. A medium level of CAD detail (~ 11,000 polygons) and ~ 3×10^6 tetrahedral elements were used to make a comparison between the estimated scaffold parameters derived from five different RVEs, thus achieving a good compromise in terms of computational time (19 min). The results are reported in Table III: the estimated volumetric flow rate and permeability values resulted in the same range as the ones obtained in the previous assessment under the same modeling parameters, thus confirming the reliability of the modeling strategy adopted.

TABLE III. VALUES OF SIMULATED FLOW RATE Q AND PERMEABILITY k FOR DIFFERENT RVEs.

RVE	Q ($\times10^{-7}$) [m^3/s]	k ($\times10^{-9}$) [m^2]
RVE-1	1.40	2.09
RVE-2	1.42	2.05
RVE-3	1.36	1.83
RVE-4	1.38	2.01
RVE-5	1.21	1.79

IV. DISCUSSION

A CFD approach based on RVEs has been used in this study to analyze the intrinsic permeability of a porous scaffold. The obtained results lay the foundations of a more sophisticated model to be used as support for further studies about flow distribution in 3D scaffolds for tissue engineering. The average permeability value obtained in the experiment was 1.71×10^{-9} m^2. This value results slightly larger than values found in [1, 20], coherently with the quite high porosity and large pores dimensions of the 3D scaffold here considered. The experimental permeability values are fairly close to the ones obtained through CFD simulations, although these are strongly dependent on the detail's degree of the CAD, as shown in Table II. This dependency is also reflected in Fig. 6, where the difference between experimental and simulated permeability of the roughest configuration (CAD model (c)) ranges from 54% to 72%. On the other hand, the error of the model with the highest degree of detail (CAD model (a)) spans from 11% to 22%, in agreement with other studies [1, 20]. In addition, there is no evident discrepancy between the CAD model (a) and (b); this aspect led to consider a medium level of CAD finish for the further tests. As it concerns the fluid domain discretization, the complexity of the geometry forced us to use tetrahedral elements instead of hexagonal ones. This feature is always present when the scaffold is highly non-homogeneous as the one considered in this work. The mesh refinement here employed is in the range of other works [19, 20], and Table II demonstrates that an increasing refinement over 3×10^6 elements produced higher computational costs but differences in results of less than 3%.

The reliability of these results was also confirmed by the second assessment, whose results are presented in Table III. Here the different RVEs showed a similar behavior, when the same degree of finish and the same number of tetrahedral elements were used. Analyzing multiple RVEs allowed checking the homogeneity of the scaffold in terms of fluidic behavior.

A strong limitation of the RVEs approach consists of the boundary conditions defined in the model. A no-slip condition was imposed on the four lateral sides of the RVE: this prevented any lateral flow across the walls. However, this is a fictitious condition not describing the real flow [19]. This is actually a source of error that leads to a loss of accuracy. The modification of the geometry due to the RVE and the application of no-real boundary conditions make the model of the scaffold different from the original one coming from the μCT. This is probably the reason why the estimated permeability values move away from the experimental ones, when increasing the mesh refinement (Fig. 6).

It is worth making a consideration on the computational costs. The CFD approach based on RVEs presented in this work resulted in reasonable CPU time as shown in Table II. However, the times presented in this table express merely the simulation times, though the main advantage of the RVE approach lays in the geometry reconstruction and meshing procedures. These issues could result particularly hard to face if the whole ~ 1 cm^3 scaffold should be considered, instead of portions of it. In those case, extremely powerful machines as high-performance computers or clusters would be needed [16, 28].

In this work the intrinsic permeability has been used as the only metric of assessment between the experimental

measurments and the computational model. However, this metric could result insufficient when other features of the fluid-scaffold system are taken into account, such as the wall-shear stress or the velocity distribution throughout the pores. A validation through these features would require a more complex experimental set-up, but would allow the creation of more effective and trustworthy computational models.

V. Conclusions

The influence of different modeling parameters on the prediction of scaffold permeability was investigated in this work. In particular, the degree of detail of the CAD file (number of triangular polygons) and the number of tetrahedral elements of the mesh were considered. The predictions in terms of scaffold permeability obtained through CFD simulations were compared to the experimental measurements. Results showed a strong dependency of the simulated permeability from the CAD degree of finish and, therefore, the importance of the scaffold 3D geometry reconstruction. Models with a higher degree of detail showed high result accuracy. These results lay the basis for further studies encompassing other parameters and full-scale scaffold models.

References

[1] M.C. Varley, S. Neelakantan, T.W. Clyne, J. Dean, R.A. Brooks, and A.E. Markaki. Cell structure, stiffness and permeability of freeze-dried collagen scaffolds in dry and hydrated states. *Acta biomaterialia*, 33:166–175, 2016.

[2] T. S. Karande, J. L. Ong, and C. M. Agrawal. Diffusion in musculoskeletal tissue engineering scaffolds: design issues related to porosity, permeability, architecture, and nutrient mixing. *Annals of biomedical engineering*, 32(12):1728–1743, 2004.

[3] A. A. Al-Munajjed, M. Hien, J. P. Kujat, R. Gleeson, and J. Hammer. Influence of pore size on tensile strength, permeability and porosity of hyaluronan-collagen scaffolds. *Journal of Materials Science: Materials in Medicine*, 19(8):2859–2864, 2008.

[4] M. V. Chor and W. Li. A permeability measurement system for tissue engineering scaffolds. *Measurement Science and Technology*, 18(1):208, 2006.

[5] F. Iberite, I. Gerges, L. Vannozzi, A. Marino, M. Piazzoni, T. Santaniello, C. Lenardi, and L. Ricotti. Combined effects of electrical stimulation and protein coatings on myotube formation in a soft porous scaffold. *Annals of biomedical engineering*, 48(2):734–746, 2020.

[6] I. Ochoa, J.A. Sanz-Herrera, J. M. Garcıa-Aznar, M. Doblare, D.M. Yunos, and A. R. Boccaccini. Permeability evaluation of 45s5 bioglass R -based scaffolds for bone tissue engineering. *Journal of biomechanics*, 42(3):257–260, 2009.

[7] B.-S. Kim, A.J. Putnam, T. J. Kulik, and D. J. Mooney. Optimizing seeding and culture methods to engineer smooth muscle tissue on biodegradable polymer matrices. *Biotechnology and bioengineering*, 57(1):46–54, 1998.

[8] D. Sin, X. Miao, G. Liu, F. Wei et al.. Polyurethane (PU) scaffolds prepared by solvent casting/particulate leaching (SCPL) combined with centrifugation. Mater. Sci. Eng. C 30, 78, 2010.

[9] B.J. Lawrence, S.V. Madihally. Cell colonization in degradable 3D porous matrices. *Cell adhesion & migration*, *2*(1), 9–16. https://doi.org/10.4161/cam.2.1.5884, 2008.

[10] C. E. Holy, M. S. Shoichet, and J. E. Davies. Engineering three-dimensional bone tissue in vitro using biodegradable scaffolds: Investigating initial cell-seeding density and culture period. *Journal of Biomedical Materials Research,* 51(3):376–382, 2000.

[11] D. Ali, M. Ozalp, S. B.G. Blanquer, and S. Onel. Permeability and fluid flow-induced wall shear stress in bone scaffolds with tpms and lattice architectures: A cfd analysis. *European Journal of Mechanics-B/Fluids*, 79:376–385, 2020.

[12] S. Gomez, M.D. Vlad, J. Lopez, and E. Fernandez. Design and properties of 3d scaffolds for bone tissue engineering. *Acta biomaterialia*, 42:341–350, 2016.

[13] S. Truscello, G. Kerckhofs, S. Van Bael, G. Pyka, J. Schrooten, and H. Van Oosterwyck. Prediction of permeability of regular scaffolds for skeletal tissue engineering: a combined computational and experimental study. *Acta biomaterialia*, 8(4):1648–1658, 2012.

[14] D. Ali and S. Sen. Finite element analysis of mechanical behavior, permeability and fluid induced wall shear stress of high porosity scaffolds with gyroid and lattice-based architectures. *Journal of the mechanical behavior of biomedical materials*, 75:262–270, 2017.

[15] A. Lesman, Y. Blinder, and S. Levenberg. Modeling of flow-induced shear stress applied on 3d cellular scaffolds: Implications for vascular tissue engineering. *Biotechnology and bioengineering*, 105(3):645–654, 2010.

[16] A. J.F. Stops, K.B. Heraty, M. Browne, F. J. O'Brien, and P.E. McHugh. A prediction of cell differentiation and proliferation within a collagen– glycosaminoglycan scaffold subjected to mechanical strain and perfusive fluid flow. *Journal of biomechanics*, 43(4):618–626, 2010.

[17] F. P.W. Melchels, B. Tonnarelli, A. L. Olivares, I. Martin, D. Lacroix, J. Feijen, D. J. Wendt, and D. W. Grijpma. The influence of the scaffold design on the distribution of adhering cells after perfusion cell seeding. *Biomaterials*, 32(11):2878–2884, 2011.

[18] I. Papantoniou, Y. Guyot, M. Sonnaert, G. Kerckhofs, F. P. Luyten, L. Geris, and J. Schrooten. Spatial optimization in perfusion bioreactors improves bone tissue-engineered construct quality attributes. *Biotechnology and bioengineering*, 111(12):2560–2570, 2014.

[19] F. Zhao, J. Melke, K. Ito, B. van Rietbergen, and S. Hofmann. A multiscale computational fluid dynamics approach to simulate the micro-fluidic environment within a tissue engineering scaffold with highly irregular pore geometry. *Biomechanics and modeling in mechanobiology*, 18(6):1965– 1977, 2019.

[20] V. A. A. Santamarıa, M. Malve, A. Duizabo, A. M. Tobar, G. G. Ferrer, J.M. G. Aznar, M. Doblare, and I. Ochoa. Computational methodology to determine fluid related parameters of non regular three-dimensional scaffolds. *Annals of biomedical engineering*, 41(11):2367–2380, 2013.

[21] C. Sandino, J.A. Planell, and D. Lacroix. A finite element study of mechanical stimuli in scaffolds for bone tissue engineering. *Journal of biomechanics*, 41(5):1005–1014, 2008.

[22] I. Gerges, M. Templenizza, F. Martello, C. Recordati, C. Martelli et al.. Exploring the potential of polyurethane-based soft foam as cell-free scaffold for soft tissue regeneration. *Acta Biomaterialia,* 73:141-153, 2018.

[23] Elettra and FERMI lightsources. Tomolab. http://www.elettra.trieste.it.html.

[24] N. Otsu. A threshold selection method from gray-level histograms. *IEEE trans on systems, man, and cybernetics*, 9(1):62–66, 1979.

[25] M. M. Doube, M.and Kłosowski, I. Arganda-Carreras, F. P. Cordelieres, R.P. Dougherty, J. S Jackson, B. Schmid, J.R. Hutchinson, and S. J. Shefelbine. Bonej: free and extensible bone image analysis in imagej. *Bone*, 47(6):1076–1079, 2010.

[26] J. Schindelin, I. Arganda-Carreras, E. Frise, V. Kaynig, M. Longair, T. Pietzsch, S. Preibisch, C. Rueden, S. Saalfeld, B. Schmid, et al. Fiji: an open-source platform for biological-image analysis. *Nature methods*, 9(7):676–682, 2012.

[27] ThermoFisher Scientific. Amira. https://www.thermofisher.com.

[28] C. Jungreuthmayer, M. J. Jaasma, Am. A. Al-Munajjed, J. Zanghellini, D. J. Kelly, and F. J. O'Brien. Deformation simulation of cells seeded on a collagen-gag scaffold in a flow perfusion bioreactor using a sequential 3D CFD-elastostatics model. *Medical engineering & physics*, 31(4):420–427, 2009.

[29] P. Cignoni, M. Callieri, M. Corsini, M. Dellepiane, F. Ganovelli, G. Ranzuglia. MeshLab: an Open-Source Mesh Processing Tool. Sixth Eurographics Italian Chapter Conference, page 129-136, 2008.

[30] Autodesk.co.uk. 2018. Cloud Powered 3D CAD/CAM Software for Product Design | Fusion 360.